3D Printing of Functional Mesoporous Silica Monoliths with Embedded Metal and MOF Components

ADVANCED FUNCTIONAL MATERIALS
www.afm-journal.de

3D Printing of Functional Mesoporous Silica Monoliths with Embedded Metal and MOF Components

*Thomas Gaillard, Arianna Bertero, Christine Joly-Duhamel, Christine Biolley, Bartolomeo Coppola, Nicolas Brun, Anne Galarneau, and Tangi Aubert**

The advent of 3D printing has transformed the field of manufacturing, offering unprecedented opportunities to create complex structures. Digital light processing (DLP)-based stereolithography has been widely adopted by material scientists, and DLP printers are now commonly available. However, despite its innovative nature, 3D printing remains limited in terms of material compatibility, which has largely been restricted to organic polymers and their composite derivatives. The direct printing of inorganic and functional structures remains challenging. To expand the potential of 3D printing to a broader spectrum of emerging materials, a new type of inks based on photo-cross-linkable nanoparticles is developed. Specifically, silica nanocages functionalized with methacrylate ligands enable the direct printing of mesoporous silica monoliths, eliminating the need for additional organic binders or calcination. Innovative functionalized inks are further developed by adding metal salts (Co, Ni, Cu, and Pd) into the silica inks allowing the selective positioning of different metallic zones along a monolith. In addition, a complementary strategy is presented for the in situ growth of microporous metal-organic frameworks (HKUST-1) within printed mesoporous silica monoliths. These fabrication strategies pave the way for designing hierarchical architectures suitable for a wide range of catalytic and environmental applications, including reactors for cascade reactions and CO_2 capture.

1. Introduction

As scientific literature continues to report an increasing variety of materials that can be processed using 3D printing, the field has been thriving in recent years.[1,2] This innovative additive manufacturing technique enables the creation of highly intricate structures with unparalleled freedom of design, while offering numerous advantages over conventional manufacturing methods and generating tremendous opportunities in materials science. As a result, a wide range of complementary 3D printing technologies are being developed for various applications, from biomedical devices to energy materials.[3,4] Among these techniques, stereolithography by digital light processing (DLP) is a highly versatile method, allowing for the fast and simultaneous printing of multiple parts, with resolutions ranging from tens of micrometers for commonly available printers, down to few micrometers only for high-resolution ones.[5] In the classic approach, a DLP printer utilizes a digital micromirror device (DMD) to project UV light patterns toward a resin vat, locally inducing polymerization and formation of a solid layer with programmed shape. Multiple layers are then printed successively on top of each other by moving the printing platform until the desired 3D structure is obtained. As illustrated in **Figure 1d**, most commercially available DLP printers use a so-called bottom-up configuration where the light patterns are projected upward from under the vat, which has a transparent bottom made of a non-sticky fluorinated polymer film. In this configuration, the layers are printed on the platform facing down and moved upward, which allows printing parts with heights exceeding the level of resin in the vat. In a commercial DLP printer, this process of successive pattern projection and platform movement is fully automatized, allowing for the fabrication of objects made of large numbers of very thin layers, typically 50 µm, with well-defined macrostructures.

While this method is primarily developed for polymeric materials,[6,7] its great versatility has motivated the development of a number of composite resins for the fabrication of advanced parts from a variety of inorganic materials, including ceramics, glass, as well as complex metamaterials.[8–11] In this composite approach, organic monomers and cross-linkers are used as

T. Gaillard, C. Joly-Duhamel, C. Biolley, N. Brun, A. Galarneau, T. Aubert
ICGM
Univ Montpellier
CNRS
ENSCM
Montpellier 34000, France
E-mail: tangi.aubert@umontpellier.fr
A. Bertero, B. Coppola
INSTM R.U PoliTO-LINCE Laboratory
Department of Applied Science and Technology
Politecnico di Torino
Turin 10129, Italy

The ORCID identification number(s) for the author(s) of this article can be found under https://doi.org/10.1002/adfm.202509897

DOI: 10.1002/adfm.202509897

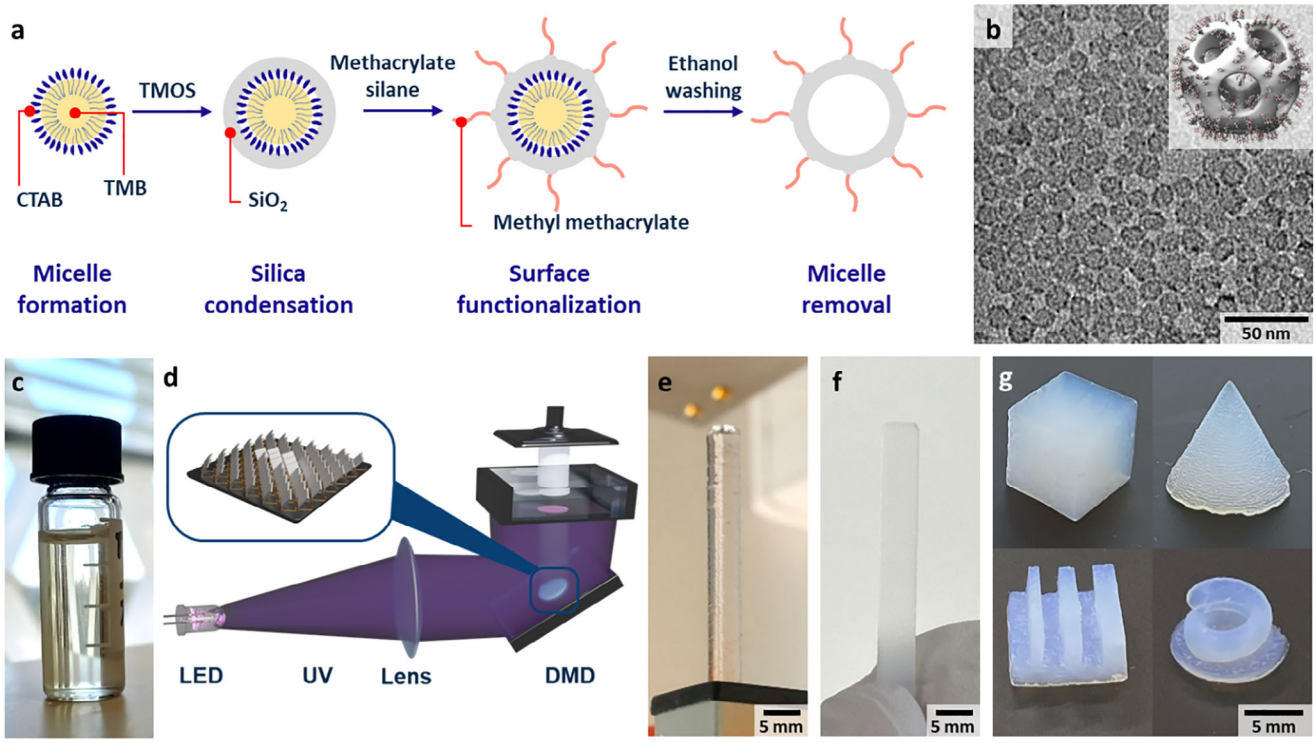

Figure 1. a) Synthesis schematic and b) TEM image of methacrylate-functionalized silica nanocages (inset: illustration of a silica nanocage). c) Picture of a silica nanocage ink solution. d) Schematic of DLP printing. Pictures of a 4 cm tall cylinder e) after printing and f) after drying. g) Pictures of printed parts with varying shapes.

binders for the inorganic filler to provide mechanical support to the printed structure. However, the resulting polymer matrix typically shows limited thermal stability, restricting their use in high-temperature environments. This approach therefore often involves a debinding or calcination step to remove the majority organic fraction, which can compromise the structural features of the object. In this context, the 3D printing of porous materials offers significant potential for a range of applications, including tissue engineering, insulating materials, catalysis, and environmental remediation,[12–15] but also comes with its own set of challenges. In particular, 3D printing could be highly valuable for the manufacturing of hierarchically porous monolithic reactors used in flow catalytic, sensing, or environmental applications.[16–18] This fabrication strategy allows for the direct integration of fully programmable macro-channels within these reactors, enhancing fluid transport, preventing pressure drop, and improving surface accessibility. This advanced reactor design can be further enhanced with the addition of acid sites, metals, or hybrid metal-organic frameworks (MOFs) to selectively perform reactions or capture species.[19,20] However, controlling the porosity at multiple scales while maintaining structural and functional integrity remains a delicate task. Using large fractions of polymer binder would strongly hinder pore accessibility and any calcination or sintering process should be avoided to preserve the smallest pores and potential organic functions of interest. Thus, new printing formulations, compatible with standard stereolithography printers are needed to unlock the full potential of 3D-printed hierarchical and functional monoliths.

In alternative to this composite resins, an innovative approach is emerging for the printing of advanced functional materials from inks of colloidal photo-cross-linkable nanoparticles.[21–23] In particular, nano-inks of ultrasmall (≈10 nm) silica nanocages functionalized with photosensitive methacrylate ligands have enabled the direct printing of intrinsically porous parts.[24] This approach contrasts significantly with the conventional composite approach by reducing the organic fraction to its bare minimum, that is the photosensitive ligands. As a result, the porosity and large surface area of the material are readily accessible without any calcination step required. The direct printing of mesoporous materials from methacrylate-functionalized silica nanocages inks therefore constitute a promising platform for the fabrication of hierarchical monolithic reactors. However, the initial proof-of-concept relied on a manually run UV DLP projector operating in a top-down configuration, i.e., with the light pattern projected from above the vat, which severely limited the fabrication process to a small number of layers with poorly controlled thickness.[24]

To overcome these limitations, in this work, we demonstrate the automated printing of large structures (cylindrical mesoporous silica monoliths) with a virtually unlimited number of layers using a standard bottom-up DLP printer, by optimizing the silica nanocage inks and printing parameters. We further showcase the high versatility of the process and added value of the 3D printing process for the implementation of functionalities within the material, capitalizing on their intrinsic porosity, either through further modification of the inks or through post-printing processes. These strategies allowed in particular the

localized positioning of various metallic sites (Co, Ni, Cu, and Pd) or the in situ growth of MOFs (HKUST-1) within the silica monoliths, which pave the way for functional applications such as one-pot cascade reactions in heterogeneous catalysis and CO_2 capture technologies.

2. Results and Discussion

2.1. Formulation of the Silica Nanocage Printing Inks

Although the bottom-up configuration of typical DLP printers enables the fabrication of large 3D structures from shallow ink levels in the vat, a substantial ink supply remains highly desirable, particularly for compatibility with printers featuring large vats and print platforms. To this end, the synthesis of silica nanocages and the ink formulation process were modified from previous work[24] to make them relevant for large-scale and automated printing. First, the synthesis of the methacrylate-functionalized nanocages around hexadecyltrimethylammonium bromide (CTAB) micelles swollen with mesitylene (TMB), illustrated in Figure 1a, was seamlessly scaled up to the liter scale (see Experimental Section). This process yielded uniform nanoparticles with an average size of 13 nm and exhibiting the same structure as the nanocages synthesized in smaller batches (Figure 1b), which were demonstrated to feature a dodecahedral symmetry.[25] In line with the scale-up of the synthesis, the purification method also had to be adapted. In the original synthesis method, the CTAB micelles were removed through a lengthy dialysis process, involving very large volumes of solvent and thereafter of waste, which was not suited for large-scale syntheses. Here, the as-synthesized methacrylate-functionalized nanocages were first precipitated from the reaction medium by the addition of ethanol, and could then be easily collected by standard centrifugation. Once separated from the aqueous liquid phase, the nanocages could then be dispersed in ethanol, forming a clear and stable suspension. The ability to first precipitate the nanocages with ethanol and then disperse them in that same solvent is a strong indication that the CTAB micelles have been effectively removed during the process. Adding ethanol to the reaction mixture dissociates the micelles, causing the methacrylate-functionalized nanocages to become unstable in the aqueous phase due to the methacrylate ligands, whereas after centrifugation the nanocages remain stable in pure ethanol. This precipitation step hence considerably helped in reducing the process time and waste generation. The silica nanocages were further concentrated and washed with ethanol using centrifugal concentrators. The removal of the structuring micelles was confirmed through Fourier transform infrared spectroscopy (FTIR) (Figure S1, Supporting Information).

For the formulation of the printing inks, propylene carbonate was used as the solvent, which was found to be suitable for the dispersion of the methacrylate-functionalized silica nanocages. Propylene carbonate offers greater safety[26] compared to other solvents used in previous work, such as alcohols and toluene, which are flammable and toxic. It is also non-volatile, which prevents solvent evaporation during long print jobs, and its high boiling point allows to easily transfer the silica nanocages from ethanol to propylene carbonate using a rotary evaporator. The photoinitiator, mainly diphenyl(2,4,6-trimethylbenzoyl)phosphine oxide (TPO) in this work, is then dissolved directly in the propylene carbonate solution containing the nanocages, yielding clear nano-inks ready for printing (Figure 1c). All the ink compositions investigated in this work, with varying nanocage or photoinitiator concentrations, exhibited excellent colloidal stability with long shelf life when stored in the dark.

2.2. Automated DLP Printing of Large Monolithic Structures

These silica nanocage inks were made compatible with standard bottom-up DLP printers, enabling the automated fabrication of large monoliths composed of hundreds of layers (Figure 1e). After solvent removal by critical point drying, the printed parts show slight scattering (Figure 1f), which already indicates substantial intrinsic porosity. This streamlined 3D printing process using silica nanocages enables the fabrication of complex objects with diverse geometries, including sharp edges, inclined surfaces, and rounded features (Figure 1g). To achieve this result, a number of printing parameters had to be optimized. Despite the many advantages of bottom-up configurations in DLP printing, they also present certain technical challenges. Under these conditions, the printed structure must have sufficient mechanical cohesion to withstand the peeling forces generated during the separation of each layer from the bottom of the vat. To prevent part breakage during printing due to such peeling forces, the lift speed of the platform was here limited to 1 mm min^{-1} during printing. The platform was also raised by 1 mm between each layer to allow for ink recoating, resulting in print times of 20 min per millimeter. Another key factor in the printing process is the light dose received by each layer, which, in combination with the photoinitiator concentration, are the primary parameters governing the cross-linking of the methacrylate-functionalized silica nanocages and, consequently, the macroscopic cohesion of the printed part. On one hand, insufficient light exposure or photoinitiator concentration can result in poor mechanical resistance and eventually in part breakage during printing. On the other hand, excessive light exposure and unrestricted photo-reaction can cause overcuring, i.e., solidification of the ink outside of the intended pattern. To find the balance between these parameters, a series of small 6 mm tall cylindrical monoliths were printed at varying photoinitiator concentrations and light doses (**Figure 2**). For these prints, the silica nanocage concentration was set to 200 mg mL^{-1}, which was determined by parallel experiments (outlined below) to be a good concentration for printing. Figure 2 shows that the limiting conditions to obtain complete prints with well-defined shapes are either a combination of [TPO] = 30 mM with a light dose of 10 mJ cm^{-2}, or [TPO] = 20 mM with a light dose of 15 mJ cm^{-2}. For the remainder of this work, the latter option was chosen as an optimal balance between chemical usage and print quality. For TPO concentrations below 20 mM, we could not identify satisfying printing conditions, as increasing the light dose above 15 mJ cm^{-2} typically resulted in overcuring. Interestingly, however, we also observed that a high photoinitiator concentration (e.g., [TPO] = 30 mM in Figure 2) can reduce lateral overcuring. Considering the low light scattering from 13 nm silica nanocages, it is believed that lateral overcuring observable at low TPO concentration is rather due to the diffusion of

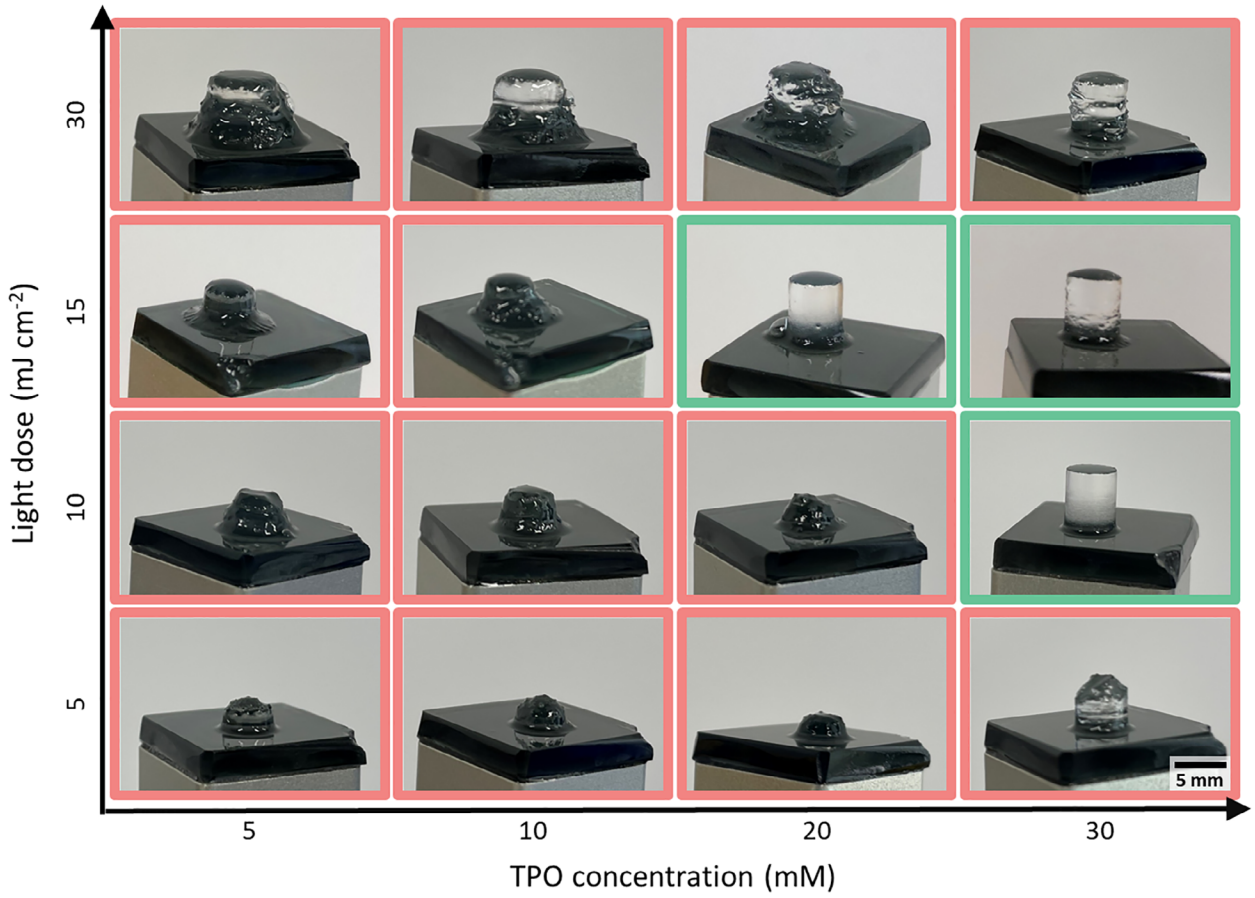

Figure 2. Pictures of cylindrical monoliths printed at different photoinitiator (TPO) concentrations and light doses. The printing model is a 5×6 mm cylinder. Good printing conditions are highlighted in green and bad ones in red.

photo-generated radicals. The reduced overcuring at high TPO concentration can therefore be explained by a concomitant increase in radical deactivation probability.[27] TPO was initially chosen as the photoinitiator based on prior work,[24] but it is worth noting that alternative photoinitiators can also be employed. Inks formulated with phenylbis(2,4,6-trimethylbenzoyl)phosphine oxide (BAPO) for instance, which has absorption properties comparable to TPO at 385 nm (Figure S2, Supporting Information), yielded similar results (Figure S3, Supporting Information), including the reduced overcuring at higher photoinitiator concentrations. BAPO actually offers an even broader range of good printing conditions, with successful prints starting from [BAPO] = 20 mM and light dose = 10 mJ cm^{-2}. Thus, while not the primary photoinitiator used in this study, BAPO could prove to be a more effective choice in future work.

2.3. Influence of the Silica Nanocage Ink Concentration

Next to the photoinitiator concentration and light dose, another parameter of high importance for printability is the silica nanocage concentration. We therefore prepared inks with varying silica nanocage concentration, ranging from 100 to 250 mg mL^{-1}, to print 40 mm tall cylindrical monoliths while keeping the other parameters constant ([TPO] = 20 mM, light dose: 15 mJ cm^{-2}). Attempts to further increase the concentration resulted in the solidification of the ink after a few days, likely due to the condensation of residual silanol groups between nanocages, making such formulations non-suitable for 3D printing applications. **Figure** 3a shows that the structure could be successfully printed all the way using formulations with nanocage concentrations between 150 and 200 mg mL^{-1}. At lower concentrations, the structure typically broke off early in the printing process due to a lack of mechanical cohesion in the formed object, similar to the issue observed for insufficient light dose or photoinitiator concentration (Figure 2). For inks with silica nanocage concentrations above 200 mg mL^{-1}, however, the structure could be partially printed but eventually broke off after about a centimeter. To explain this breakage behavior at late stage of the printing process, the rheological properties of the different formulations were analyzed, revealing a steep increase in the ink viscosity for nanocage concentrations exceeding 200 mg mL^{-1} (Figure 3b). Structure breakage observed for high-concentration inks may then be attributed to this abrupt change in the ink rheology, which could hinder the ink recoating between layers or induce important dragging forces on the printed part during printing platform movement. At a given nanocage concentration, however, the ink rheological properties also

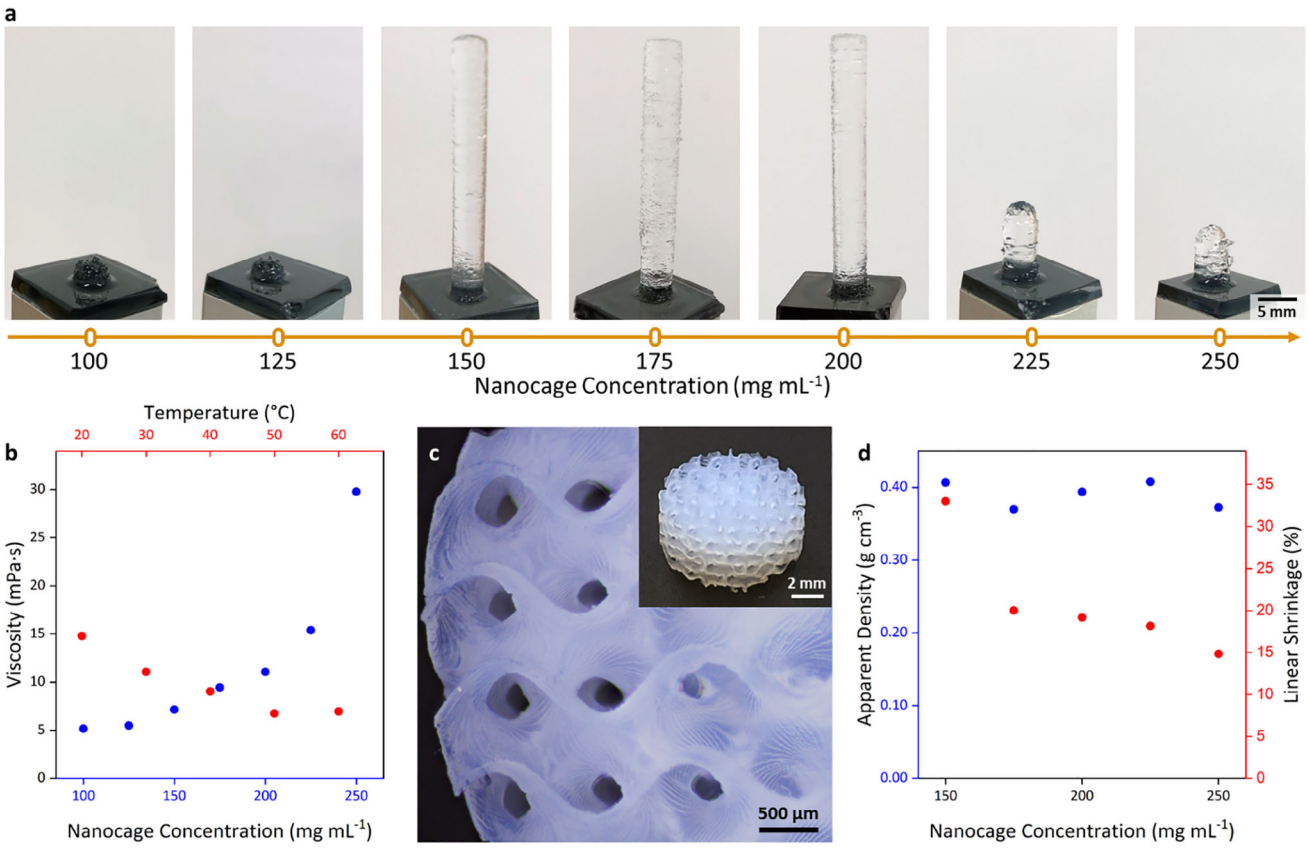

Figure 3. a) Pictures of cylindrical monoliths printed at different silica nanocage concentrations. **b**) Viscosity of the ink as a function of nanocage concentration (temperature: 30 °C, shear rate: 13 s^{-1}), and as a function of temperature (silica nanocage concentration: 200 mg mL^{-1}, shear rate: 13 s^{-1}). **c**) Stereomicroscopy image of a monolith featuring a Gyroid structure printed from an ink with a silica nanocage concentration of 300 mg mL^{-1} and stabilized with Disperbyk-168 TF (inset: picture of the whole monolith). **d**) Apparent density and linear shrinkage of cylindrical monoliths after drying as a function of silica nanocage concentration. For all these experiments, the TPO concentration was set to 20 mM and the light dose to 15 mJ cm^{-2}.

depend on the temperature. Figure 3b shows that, for a 200 mg mL^{-1} ink, decreasing the temperature leads to an increase in viscosity. This relationship between temperature and rheological properties underscores the importance of thermal control. To prevent printing issues related to ink viscosity, especially in colder winter conditions for instance, the ink vat was therefore maintained at a constant 30 °C for all printing jobs, using a controlled heating band applied directly on the vat. This ensured that fluctuations in ambient temperature did not affect the ink performance. To alleviate the limit in nanocage concentration due to the ink viscosity, a dispersant, namely Disperbyk-168 TF, was added to the ink formulation. The addition of 36 mg mL^{-1} of Disperbyk-168 TF allowed to increase the silica nanocage concentration to 300 mg mL^{-1}, while maintaining good colloidal stability over time and suitable viscosity. This optimized ink enabled the successful printing of a monolith with an intricate Gyroid macroporous structure (Figure 3c).

2.4. Structural and Textural Properties of Printed Silica Monoliths

For inks without dispersant, small cylindrical monoliths (5 × 6 mm) could be printed from silica nanocage concentrations ranging from 150 to 250 mg mL^{-1}. The weight of the silica monolith after drying appeared to increase with the ink concentration, even though it was printed from the same 3D model. However, while the dimensions of all printed silica monoliths showed high fidelity to the model right out of the printer, isotropic shrinkage was observed after drying with supercritical CO_2. This shrinkage depended on the ink concentration (Figure 3d), from 15% at high concentration (250 mg mL^{-1}) to 30% at low concentration (150 mg mL^{-1}). Interestingly, all the printed silica monoliths after drying actually exhibit a constant apparent density of ≈0.4 g cm^{-3}, regardless of the ink concentration (Figure 3d), meaning that the shrinkage compensates the initial difference in density. The organic fraction (i.e., mainly the methacrylate ligands) of the silica monoliths after drying was estimated to 36 wt.% by TGA analyses (Figure S4, Supporting Information). Assuming standard densities of 2.2 and 1.2 g cm^{-3} for the amorphous silica and organic ligands, respectively, this apparent density suggests that the porosity (V_{pore}/V_{total}) of the silica monoliths is close to 0.8. The mechanical properties of such 3D-printed porous monoliths were evaluated through compressive testing and compared with those of more conventional porous monoliths fabricated via sol-gel synthesis combined with spinodal decomposition,[16] which are developed for continuous

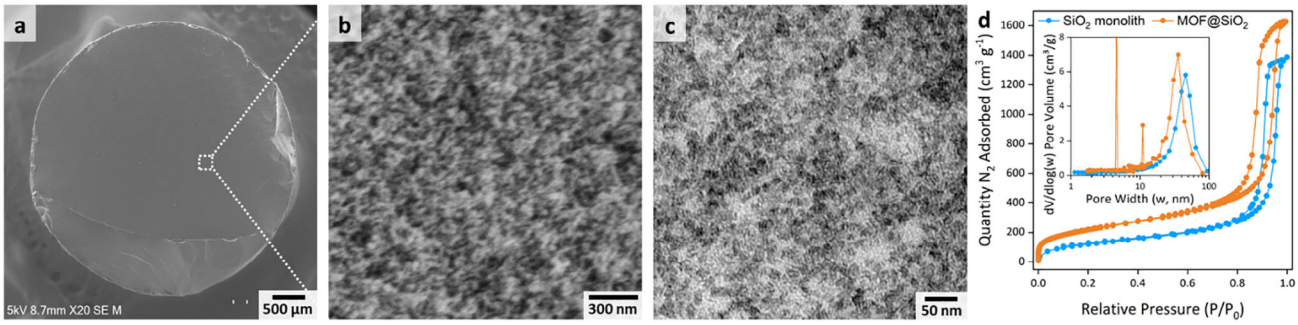

Figure 4. Structural characterization of a monolith printed with a nanocage concentration of 200 mg mL^{-1}, including **a,b**) SEM images showing the inside of the fractured monolith at different magnifications, **c**) TEM image of a microtome section of the printed material, and **d**) N_2 sorption isotherms (inset: pore size distributions as determined by the BJH method from the adsorption branch).

flow processes. The 3D-printed monolith demonstrated significantly higher resistance (Figure S5, Supporting Information), exhibiting a compressive strength of nearly 1 MPa for a sample printed with a silica nanocage concentration of 200 mg mL^{-1}, in contrast to 0.4 MPa for the sol-gel-derived monoliths. The elastic modulus was also estimated from the linear section of the stress-strain curves (Figure S5, Supporting Information), resulting in values of 10 and 27 MPa for the 3D-printed and sol-gel monoliths, respectively.

The low apparent density of 3D-printed monoliths originates from the intrinsic porosity of the nanocages, as well as from the interparticle porosity formed between the nanocages during printing. Indeed, while low magnification scanning electron microscopy (SEM) images of a fractured silica monolith evidence a largely homogeneous structure without defects or cracks (**Figure** 4a), higher magnification SEM images (Figure 4b) show significant interparticle porosity. Transmission electron microscopy (TEM) observations of microtome sections (Figure 4c) further evidence that the intraparticle porosity of the nanocage is also preserved.

The textural properties of the silica monoliths were further characterized by nitrogen sorption at 77 K. The isotherms (Figure 4d; Figure S6, Supporting Information) are of type IV with a capillary condensation at ca. $P/P_0 = 0.95$ and a desorption at ca. $P/P_0 = 0.90$, typical of mesoporous materials with large mesopores. All silica monoliths exhibited a specific surface area S_{BET} comprised between ≈400 and 500 $m^2\ g^{-1}$, and a mesopore volume between 1.3 and 2.2 mL g^{-1} (Table S1, Supporting Information) with no clear correlation with the ink concentration and S_{BET} values. For example, the silica monolith printed with a silica nanocage concentration of 200 mg mL^{-1}, features a S_{BET} of 450 $m^2\ g^{-1}$ and a mesopore volume of 2.1 mL g^{-1} (Figure 4d). From the SEM and TEM images (Figure 4b,c), it is clear that the monolith porosity consists of highly constricted pores. In this case, pore sizes are better estimated by applying the Barrett-Joyner-Halenda (BJH) model to the adsorption branch of the isotherms.[28] The results indicate mesoporosity with a broad distribution in the 30–60 nm range (inset Figure 4d; Figure S6, Supporting Information). The BJH method relies on assumptions about pore geometry that may not accurately represent our system. Nevertheless, this result suggests that the pore volume is predominantly influenced by interparticle porosity. While the internal porosity of the nanocages may contribute to the specific surface area, it does not add significantly to the overall pore volume.

It should be noted that while the porosity and large surface area are readily accessible after printing and drying, the material can be calcined without affecting their textural properties. After calcination at 550 °C for 6 h, the overall shape of nitrogen isotherms is similar to the one of as-dried silica monoliths (Figure S7, Supporting Information) with higher surface area and pore volume due to the elimination of the organics. Indeed, specific surface area and pore volume are expressed per mass of materials and not per mass of silica, which will be the case for a calcined monolith. For example, a surface area of 450 $m^2\ g^{-1}$ for the previous dried silica monolith expressed per mass of material will correspond to ≈700 $m^2\ g^{-1}$ per mass of silica. This value agrees with the S_{BET} determined from the nitrogen isotherms of calcined silica monoliths (Table S1, Supporting Information) and is consistent with previous work.[24]

2.5. 3D-Printed Functional Monoliths

In previous sections, we have demonstrated the 3D printing of monolithic structures from silica nanocages. These silica monoliths possess high porosity and their macroscopic size and shape can be fully tailored thanks to the 3D printing capabilities. These structures might hold important potential for catalytic or environmental applications. However, for such applications it is essential to integrate active sites or specific functionalities. To achieve this, we have successfully developed two distinct yet complementary approaches for the implementation of functionalities in silica, either directly during the 3D printing process or through a post-printing modification method.

First, mesoporous silica is a valuable support material for catalysts such as metals (Cu,[29] Ni,[30] Pd,[31]...). Herein, we developed a straightforward approach to integrate metals into our 3D silica structures directly from the printing step, simply by dissolving metal salts, namely cobalt(II) chloride, palladium(II) acetylacetonate, nickel(II) chloride or copper(II) nitrate trihydrate in the silica nanocage ink. The silica nanocage synthesis and ink preparation were unchanged except that 1-methyl-2-pyrrolidinone (NMP) was used as the solvent instead of propylene carbonate in order to allow for higher salt concentrations in the inks (see Experimental Section). These inks could be

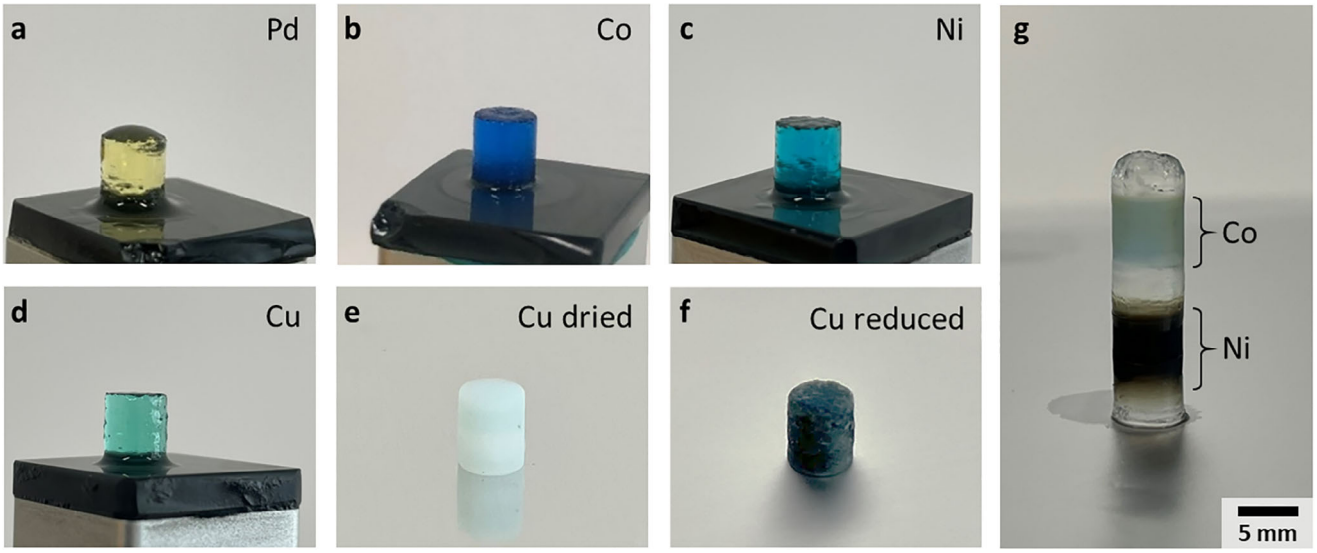

Figure 5. Pictures of functional silica monoliths printed from nanocage inks containing metal salts, including a) Pd, b) Co, c) Ni, and d) Cu salts. Pictures of a Cu-silica monolith e) dried as-is, and f) with in situ reduction before drying. g) Picture of a silica monolith with alternating inks of plain silica nanocages, silica nanocages with cobalt salt, and silica nanocages with nickel salt.

seamlessly used with the same printing parameters as described above for the fabrication of Pd, Co, Ni, or Cu containing monoliths (**Figure** 5a–d). While positively charged metal ions are easily adsorbed by silica gel materials due to the presence of silanol groups,[32] some leaching of the metal ions was observed during the successive washing and drying steps of the monolith fabrication process (Figure 5e). To prevent this, the metal ions can be reduced in situ immediately after printing by immersing the monolith in a solution of sodium borohydride in ethanol. Figure 5f shows the picture of a Cu containing monolith exhibiting a dark coloration, which suggests the formation of Cu-based particles that remain trapped in the porosity and are not leached out from the monolith during washing and drying steps. This allowed to increase the copper loading from 0.7 wt.% for monoliths dried as-is (Figure 5e) to 1.8 wt.% for monoliths dried after reduction (Figure 5f), as determined by inductively coupled plasma optical emission spectroscopy (ICP-OES). These monoliths were printed from inks containing 200 mg mL^{-1} of silica nanocages and 6.4 mg mL^{-1} of elemental Cu. Therefore, a loading of 1.8 wt.% is reasonably close to the theoretical maximum of 3 wt.% Cu in the dried material. These Cu-based particles in the silica monolith were observed by dark-field scanning transmission electron microscopy (DF-STEM), revealing homogeneously dispersed nanoparticles of typically 2–3 nm in size (Figure S8, Supporting Information). X-ray photoelectron spectroscopy (XPS) analyses revealed a shift of the Cu $2p_{3/2}$ peak to lower binding energies, along with the disappearance of its satellite feature at ≈942 eV following immersion of the Cu containing monolith in a $NaBH_4$ solution (Figure S9, Supporting Information). These changes are characteristic of the reduction of Cu(II) to a lower oxidation state. However, XPS alone could not differentiate between Cu(I) and Cu(0), as both species exhibit similar Cu $2p_{3/2}$ peak positions. Moreover, metallic Cu is readily oxidized upon exposure to air, meaning that applications requiring Cu(0) would necessitate an activation step under reducing conditions. To address this, temperature-programmed reduction (TPR) experiments were conducted on the Cu containing monolith, demonstrating that the Cu species could be effectively reactivated at 500 °C under a 3% H_2 atmosphere, resulting in the formation of Cu(0) as confirmed by X-ray diffraction (XRD) analyses (Figure S10, Supporting Information).

Thanks to the additive nature of the fabrication process the position of the metallic sites can further be controlled along the printed structure. Figure 5g shows the picture of a monolith in which specific sections of the structure are loaded with Co and Ni. This monolith was printed through a process of ink substitution, by alternating between a standard silica nanocage ink and Co or Ni-containing inks during printing. This 3D printing approach hence allows the deliberate positioning of various metallic sites in series along the monolith for cascade or sequential catalytic reactions requiring different active sites.[30] While the potential catalytic activity of these metallic sites remains to be demonstrated, we believe that, when integrated with macroporous networks such as the Gyroid structure shown in Figure 3c, these monoliths could serve as effective reactors for flow applications. The design of such functional heterostructures, hardly doable with conventional monolith fabrication approaches, is hence made possible by the additive manufacturing strategy.

Functionality can also be introduced in the monolith post-printing. In this other approach, we took advantage of the readily available mesoporosity of silica monoliths to infiltrate them with precursors for the in situ growth of an active phase. As a first example, a MOF (HKUST-1), was chosen as active phase. MOFs are crystalline structures with specific copper catalytic functions.[33] In addition, their well-defined microporosity offers good sorption capacity toward gases such as CO_2, making them highly valuable for carbon capture and storage technologies.[20] However, MOFs are often synthesized as powders, and need to be supported for potential applications (catalysis, adsorption) as reactors under continuous flow. The protocol for MOF in situ

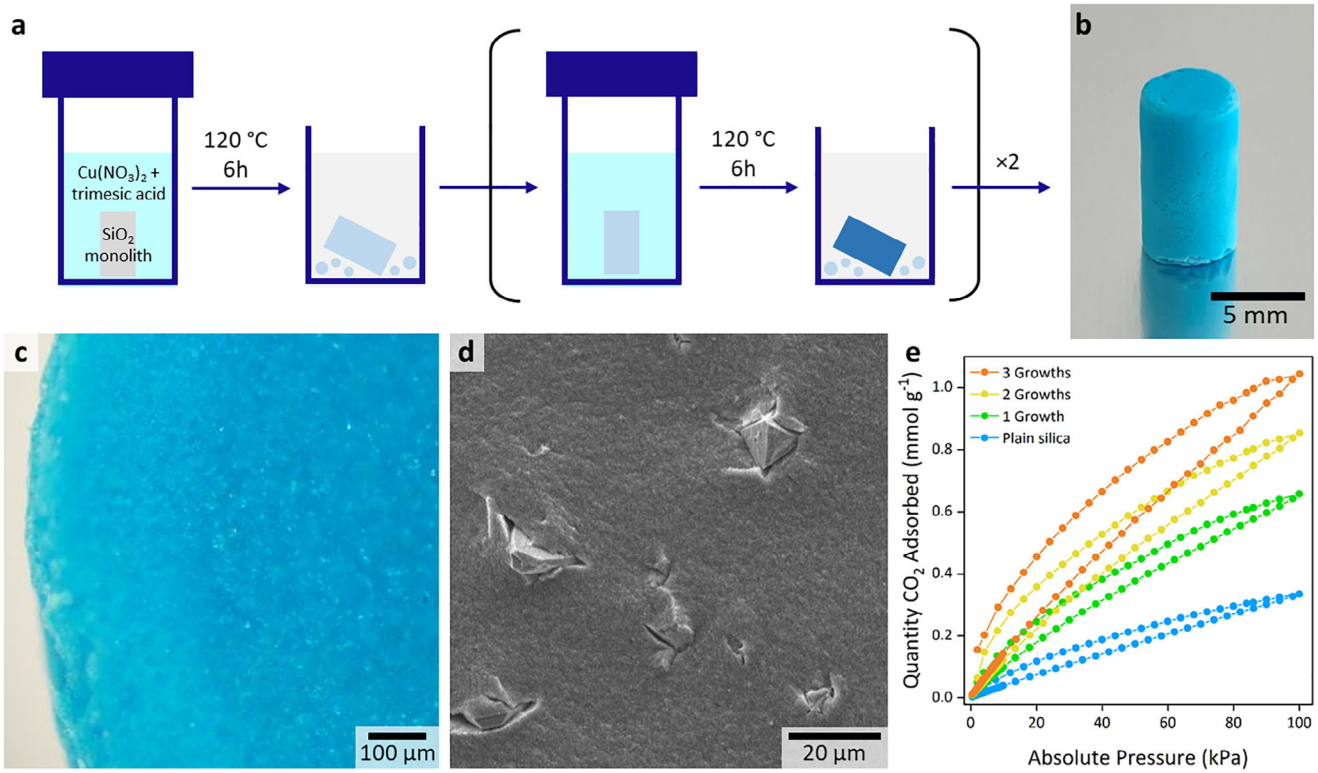

Figure 6. a) Illustration of the in situ growth of HKUST-1 in 3D-printed mesoporous silica monoliths. b) Picture, c) stereomicroscopy image, and d) SEM image of a HKUST-1 containing monolith after three successive in situ growths. e) CO_2 sorption isotherms of a plain silica monolith and after one, two, and three in situ successive HKUST-1 growths.

crystallization, illustrated in **Figure** 6a, was adapted from a previous report on the solvothermal synthesis of HKUST-1 crystals on ceramic substrates.[18] The as-printed silica monoliths were immersed in a solution of $Cu(NO_3)_2$ and trimesic acid in a Teflon lined autoclave, and the mixture was heated to 120 °C for 6 h (see Experimental section for details). This procedure was repeated twice on the same monolith, resulting in a total of three consecutive MOF growths. MOFs were hence grown directly inside printed silica monoliths. The final structure exhibited a deep blue coloration that turned to a lighter blue upon contact with humidity (Figure 6b), resembling the behavior of regular HKUST-1 powder. Stereomicroscope images evidenced a homogeneous distribution of the blue MOF crystals within the silica monolith (Figure 6c). SEM observations further revealed the presence of some larger octahedral crystals (≈15 µm), characteristic of the HKUST-1 structure, embedded within the silica matrix (Figure 6d). The HKUST-1 crystal phase was also confirmed through XRD analyses performed on crushed monoliths (Figure S11, Supporting Information). The HKUST-1 loading was estimated to account for ≈30 wt.% of the resulting monolith after three growth steps. This was determined by comparing the typical weights of a plain silica monolith with that of one containing the MOF. This in situ growth of a secondary material in the porous monolith did not alter its mesoporosity, as proven by nitrogen sorption at 77 K. The isotherms of the MOF/silica composite monoliths (Figure 4d) showed a similar overall shape as compared to the monolith before MOF growth. Additionally, N_2 adsorption at low relative pressure ($P/P_0 < 0.05$) increased substantially, which is attributed to the filling of the micropores of the MOF. As a result, the specific surface area increased significantly from ≈400–500 to 800 $m^2\ g^{-1}$ and the total pore volume increased to 2.5 mL g^{-1}. This high increase in S_{BET} is attributed to the high microporosity of the HKUST-1 crystals. Indeed, pure bulk HKUST-1 materials typically feature high S_{BET} up to 2000 $m^2\ g^{-1}$.[18,33] Thus, the in situ growth of MOF introduces an additional level of porosity to the monoliths, which now include micro- and mesoporosity. The potential of these MOF/silica composite monoliths for functional applications was demonstrated through CO_2 adsorption experiments. The CO_2 sorption isotherms of the 3D-printed structures were measured after one, two, and three successive in situ growth steps, resulting in a more than threefold increase in CO_2 sorption capacity (Figure 6e). Incorporating MOF crystals into the silica monolith increased the CO_2 uptake from 0.33 mmol g^{-1} (pure silica) to 1.0 mmol g^{-1} (composite) at 100 kPa. Under our conditions, attempting to further increase the MOF loading through additional growth steps did not lead to a significant increase in CO_2 sorption capacity, which levels off after three growth steps (Figure S12, Supporting Information). We also found that successive growths at relatively low precursor concentration is more effective than a single growth at higher concentration. For instance, a single growth at [Cu] = 150 mM (as compared to three growths at [Cu] = 15 mM in Figure 6e) resulted in an inhomogeneous distribution of larger MOF crystals within the monolith and a lower CO_2 sorption capacity (Figure S13, Supporting Information).

3. Conclusion

In this work, we have developed and optimized the formulation of silica nanocage inks that are compatible with standard bottom-up DLP printers. Further optimization of the printing parameters enabled the automated fabrication of large monolithic structures, with readily available large mesoporosity and large surface area. We also demonstrated how these nano-inks offer versatile opportunities for the functionalization of the silica monoliths toward potential catalytic reactors, e.g. through the precise positioning of metals (Co, Ni, Cu, and Pd) along the monoliths. For environmental applications, the in situ growth of MOF crystals in mesoporous silica monoliths resulted in composite materials combining meso- and microporosity, and showing high potential for CO_2 capture technologies. In future developments, these materials could leverage the design flexibility of 3D printing technologies to incorporate programmed macroporosity, enhancing their suitability for flow-based applications. We also speculate that thanks to the very small size of the employed silica nanocages and their low light scattering, these photosensitive nano-inks could be made compatible with other stereolithography techniques such as two-photon polymerization,[34] which offers very high printing resolutions. Thanks to their high modularity, materials printed from such nano-inks may therefore open a number of opportunities toward the fabrication of complex and functional structures with largely inorganic compositions beyond those showcased in this work.

4. Experimental Section

Materials: Tetramethyl orthosilicate (TMOS, 98%), 1,3,5-trimethylbenzene (TMB, 98%), ammonia solution (28–30% in water), hexadecyltrimethylammonium bromide (CTAB, >99%) and 3-(trimethoxysilyl)propyl methacrylate (TPM, 98%), propylene carbonate (PC, 99%), 1-methyl-2-pyrrolidinone (NMP, 99%), diphenyl(2,4,6-trimethylbenzoyl)phosphine oxide (TPO, 97%), phenylbis(2,4,6-trimethylbenzoyl)phosphine oxide (BAPO, 97%), cobalt(II) chloride (97%), palladium(II) acetylacetonate (99%), nickel(II) chloride (98%), copper(II) nitrate trihydrate (99%), sodium borohydride (99%), copper(II) nitrate hemi(pentahydrate) (98%), and benzene-1,3,5-tricarboxylic acid (BTC, 95%) were purchased from Sigma–Aldrich. Ethanol (96%) was purchased from Carlo Erba, and methanol (98.5%) from VWR. Disperbyk-168 TF was provided by IMCD. Deionized water with a resistivity of 18 MΩ was used throughout this work.

Silica Nanocage Synthesis and Ink Formulation: The synthesis of the silica nanocages and their functionalization with methacrylate ligands for the formulation of printing inks was adapted from previously published protocols[24,25] with minor modifications. In a typical synthesis, 12.5 g of CTAB was dissolved in 1 L of deionized water under gentle heating using a heat gun until a clear solution was obtained. Subsequently, 240 µL of ammonia solution and 10 mL of TMB were added under magnetic stirring. After 4 h at room temperature, 10 mL of TMOS was slowly added to the reaction mixture, which was then kept under stirring overnight. 10 mL of TPM was then added and the synthesis was kept under stirring for another day. The resulting nanocages were precipitated by adding twice the volume of ethanol and collected by centrifugation for 5 min at 2000 g. At this point, the nanocages could be redispersed in 200 mL of ethanol, yielding a clear and stable suspension. The dispersed nanocages were further washed twice with ethanol using centrifugal concentrators (Vivaspin 20, 100 kDa MWCO) and concentrated to a final volume of ≈50 mL of silica nanocages in ethanol solution. The silica nanocage concentration was determined by drying and weighing an aliquot of this solution. For the formulation of printing inks, a calculated volume of the nanocages in ethanol solution was mixed with propylene carbonate, depending on the targeted ink concentration and volume, and the ethanol was extracted using a rotary evaporator. With this protocol, ≈30 mL of silica nanocage ink in propylene carbonate at 200 mg mL^{-1} could typically be obtained in a single batch. Finally, a calculated amount of TPO or BAPO was dissolved in the solution depending on the targeted photoinitiator concentration to complete the ink formulation. These inks were stored in the dark at room temperature and could be used for several months without noticeable change.

DLP 3D Printing: All the parts were printed using a Micro DLP printer from microSLA, with a pixel size of 15 µm, and equipped with a 385 nm UV LED. For all the prints, the layer thickness was set to 50 µm and the vat temperature was maintained at 30 °C. The lift and down speeds of the print platform were set to 1 and 100 mm min^{-1}, respectively, with a lift height of 1 mm between layers for ink recoating. These parameters were identified as good compromises for the printing of parts from different inks with varying concentrations. The optical power was systematically set to 50 mW cm^{-2} and the light dose per layer was varied between 5 and 30 mJ cm^{-2} by adjusting the exposure time between 0.1 and 0.6 s. After printing, the parts were washed with ethanol to remove residual liquid ink and then immersed in methanol. The methanol was replaced at least three times over the course of three days to remove all propylene carbonate from the parts. Finally, the printed parts were dried using either a Quorum E3100 or a Leica EM CPD300 critical point dryer under supercritical CO_2 conditions.

Fabrication of Metal Containing Monoliths: For the formulation of inks containing metal ions, NMP was used as solvent instead of propylene carbonate, allowing to reach higher concentrations. The corresponding metal salt, namely palladium(II) acetylacetonate, nickel(II) chloride, cobalt(II) chloride, or copper(II) nitrate trihydrate, was dissolved in NMP and mixed with the ethanol nanocage solution before rotary evaporation. The quantity of salt was adjusted to reach a metal ion concentration of 100 mM in the cases of Co, Ni, and Cu species and 18 mM in the case of Pd. For the in situ reduction of metal ions, the monolith was immersed immediately after printing (i.e., before exchanging the solvent with methanol) in a solution of sodium borohydride in ethanol (0.1 M) until the bubbling had stopped. The rest of the procedure for drying was identical.

Fabrication of HKUST-1/Silica Composite Monoliths: The in situ growth of HKUST-1 crystals inside already printed monoliths was adapted from previously published protocols.[18] The monoliths were immersed immediately after printing (i.e., before exchanging the solvent with methanol) in a solution containing 70 mg of trimesic acid in 20 mL of ethanol. After 10 min under gentle stirring, a solution containing 144 mg of copper nitrate in 20 mL of water was added and the mixture was kept under stirring for another 30 min. The reaction medium, including the monoliths, was then transferred to a 80 mL Teflon-lined autoclave, which was sealed and placed in an oven at 120 °C for 6 h. The parts were washed with ethanol to remove crystals formed outside of the monoliths and the same procedure was repeated several times for the successive growth of HKUST-1 crystals. After the last growth step, the solvent was exchanged for methanol and the monolith was dried under supercritical CO_2 conditions following the same protocol as described above.

Characterization Methods: Gas sorption analyses of plain silica monoliths were conducted at 77.3 K and 298 K for N_2 and CO_2 gases, respectively, using a Tristar II Plus (Micromeritics). Prior to analyses, the samples were degassed for 6 h at 50 °C and 250 °C for as-printed and calcined parts, respectively. Silica monoliths containing HKUST-1 crystals were analyzed by nitrogen sorption using a 3Flex (Micromeritics), which allowed characterizing the MOF microporosity. In this case, the samples were degassed at 80 °C during 24 h at a pressure below 1 Pa using a Smart Vac Prep bench. For plain silica monoliths, the specific surface area (S_{BET}) was calculated using the Brunauer Emmett and Teller (BET) theory with five points. For HKUST-1/silica composite monoliths, the S_{BET} was estimated following the Rouquerol criteria, in accordance with the IUPAC recommendation for combination of type I and IV isotherms.[35] Barrett-Joyner-Halenda-Broekhoff and de Boer (BJH-BdB) model was used on the adsorption branch of isotherms for pore width estimation. Thermogravimetric analyses (TGA) were performed using a Perkin Elmer instrument under air atmosphere (O_2:N_2 = 20:80) with a heating rate of 10 °C min^{-1} in the temperature range from 35 to 800 °C. Rheological analyses were

performed using an HAAKE MARS 60 rheometer (Thermo Scientific) with a cone and plate geometry (35 mm diameter, 2° angle, 0.100 mm gap). Unless specified, the temperature was maintained at 30 °C with a Peltier module. Mechanical properties were evaluated through uniaxial compressive tests using an Instron 3366 tensile tester. Stereomicroscopy images were acquired with a Zeiss Stemi 508 microscope. Bright field transmission electron microscopy (TEM) images were acquired using a Jeol JEM-1400 Plus microscope operating at 100 kV, and dark field scanning transmission electron microscopy (DF-STEM) images were acquired using a Jeol 2200FS microscope operating at 200 kV, both from MEA platform, Université de Montpellier. Scanning electron microscopy (SEM) images were acquired using a Hitachi S4800 microscope operating at 5 kV. Powder X-ray diffraction (XRD) analyses were performed using a D8 Advance (Bruker) diffractometer equipped with a Lynx eyes detector operating at 40 kV and 40 mA, and using a Cu radiation source. FTIR spectra were acquired using a PerkinElmer Spectrum Two spectrometer. UV–vis absorption spectra were acquired using a Jasco V-670 spectrophotometer. Elemental analyses by inductively coupled plasma optical emission spectroscopy (ICP-OES) were performed using a Thermo Scientific iCAP 7400 analyzer. Prior to analysis, the samples were mineralized in a mixture of HF and HNO_3 (1:1), which was subsequently heated to 200 °C until complete evaporation. X-ray photoelectron spectroscopy (XPS) analyses were performed using a Thermo Electron ESCALAB 250 spectrometer equipped with a monochromatic Al Kα (1486.6 eV) X-ray source. The binding energy scale was calibrated using the C 1s peak at 284.8 eV. Temperature-programmed reduction (TPR) of Cu-containing silica monolith was performed using a Micromeritics Autochem II 2920 analyzer. Prior to analysis, the sample was heated to 300 °C under a 50 mL min^{-1} flow of helium and then cooled to room temperature. For the analysis, the sample was heated to 800 °C at a rate of 10 °C min^{-1} under a gas flow of 50 mL min^{-1} (H_2:Ar = 3:97).

Supporting Information

Supporting Information is available from the Wiley Online Library or from the author.

Acknowledgements

The authors acknowledge Jérémy Rodriguez and Thomas Cacciaguerra for providing technical support with XRD analyses, Bertrand Rebière for the SEM analyses, and Valérie Flaud for the XPS analyses. The authors acknowledge Franck Godiard, Véronique Viguier, and Erwan Oliviero from the MEA platform, Université de Montpellier, for the TEM experiments and sample preparation. The authors acknowledge the AETE-ISO platform, OSU-OREME/Université de Montpellier for the ICP-OES analyses. This work received funding from the Agence Nationale de la Recherche under grant number: ANR-21-CE08-0012-01. Part of the research carried out for this work was made possible thanks to the financial support of CNRS International Emerging Actions within the framework of the AMOUR project.

Conflict of Interest

The authors declare no conflict of interest.

Data Availability Statement

The data that support the findings of this study are available from the corresponding author upon reasonable request.

Keywords

additive manufacturing, flow reactors, hierarchical materials, nano-ink, SLA

Received: April 19, 2025
Revised: May 23, 2025
Published online: June 10, 2025

[1] E. M. Maines, M. K. Porwal, C. J. Ellison, T. M. Reineke, *Green Chem.* **2021**, *23*, 6863.
[2] Y. Jin, X. Li, R. I. Campbell, S. Ji, *Rapid Prototyping J.* **2018**, *24*, 801.
[3] E. Yarali, M. J. Mirzaali, A. Ghalayaniesfahani, A. Accardo, P. J. Diaz-Payno, A. A. Zadpoor, *Adv. Mater.* **2024**, *36*, 2402301.
[4] M. P. Browne, E. Redondo, M. Pumera, *Chem. Rev.* **2020**, *120*, 2783.
[5] C. Sun, N. Fang, D. M. Wu, X. Zhang, *Sensor. Actuat. A: Phys.* **2005**, *121*, 113.
[6] A. Bagheri, J. Jin, *ACS Appl. Polym. Mater.* **2019**, *1*, 593.
[7] S. C. Ligon, R. Liska, J. Stampfl, M. Gurr, R. Mülhaupt, *Chem. Rev.* **2017**, *117*, 10212.
[8] Z. C. Eckel, C. Zhou, J. H. Martin, A. J. Jacobsen, W. B. Carter, T. A. Schaedler, *Science* **2016**, *351*, 58.
[9] F. Kotz, K. Arnold, W. Bauer, D. Schild, N. Keller, K. Sachsenheimer, T. M. Nargang, C. Richter, D. Helmer, B. E. Rapp, *Nature* **2017**, *544*, 337.
[10] D. G. Moore, L. Barbera, K. Masania, A. R. Studart, *Nat. Mater.* **2020**, *19*, 212.
[11] H. Cui, D. Yao, R. Hensleigh, H. Lu, A. Calderon, Z. Xu, S. Davaria, Z. Wang, P. Mercier, P. Tarazaga, X. Zheng, *Science* **2022**, *376*, 1287.
[12] F. Zhang, Z. Li, M. Xu, S. Wang, N. Li, J. Yang, *J. Eur. Ceram. Soc.* **2022**, *42*, 3351.
[13] H. Lin, Q. Shen, M. Ma, R. Ji, H. Guo, H. Qi, W. Xing, H. Tang, *Adv. Sci.* **2025**, *12*, 2412554.
[14] S. Lawson, X. Li, H. Thakkar, A. A. Rownaghi, F. Rezaei, *Chem. Rev.* **2021**, *121*, 6246.
[15] E. Shukrun Farrell, Y. Schilt, M. Y. Moshkovitz, Y. Levi-Kalisman, U. Raviv, S. Magdassi, *Nano Lett.* **2020**, *20*, 6598.
[16] A. Galarneau, A. Sachse, B. Said, C.-H. Pelisson, P. Boscaro, N. Brun, L. Courtheoux, N. Olivi-Tran, B. Coasne, F. Fajula, *CR Chim.* **2016**, *19*, 231.
[17] R. Marie-Luce, P. Mai, F. Lerouge, Y. Cheref, S. Pierre, B. Sabot, F. Chaput, C. Dujardin, *Nat. Photon.* **2024**, *18*, 1037.
[18] A. Bertero, J. Schmitt, H. Kaper, B. Coppola, P. Palmero, J.-M. Tulliani, *Appl. Mater. Today* **2024**, *40*, 102407.
[19] H. Dory, E. Petit, S. El-Sayegh, L. Badouric, V. Castro, M. Bechelany, D. Voiry, P. Miele, L. Lajaunie, C. Salameh, *Adv. Eng. Mater.* **2025**, *27*, 2401546.
[20] G. Cai, P. Yan, L. Zhang, H.-C. Zhou, H.-L. Jiang, *Chem. Rev.* **2021**, *121*, 12278.
[21] J.-Y. Huang, H. Xu, E. Peretz, D.-Y. Wu, C. K. Ober, T. Hanrath, *Chem. Mater.* **2019**, *31*, 10017.
[22] A. Desponds, A. Banyasz, D. Chateau, A. Tellal, A. Venier, S. Meille, G. Montagnac, J. Chevalier, C. Andraud, P. L. Baldeck, S. Parola, *Small* **2021**, *17*, 2102486.
[23] N. Tarutani, M. Asanome, K. Okada, M. Takahashi, T. Minato, M. Sadakane, K. Katagiri, K. Inumaru, *J. Ceram. Soc. JPN* **2023**, *131*, 830.
[24] T. Aubert, J.-Y. Huang, K. Ma, T. Hanrath, U. Wiesner, *Nat. Commun.* **2020**, *11*, 4695.
[25] K. Ma, Y. Gong, T. Aubert, M. Z. Turker, T. Kao, P. C. Doerschuk, U. Wiesner, *Nature* **2018**, *558*, 577.
[26] M. A. Liebert, *J. Am. Coll. Toxicol.* **1987**, *6*, 23.
[27] A. Ibrahim, V. Maurin, C. Ley, X. Allonas, C. Croutxe-Barghorn, F. Jasinski, *Eur. Polym. J.* **2012**, *48*, 1475.
[28] B. Coasne, A. Galarneau, F. Di Renzo, R. J. M. Pellenq, *J. Phys. Chem. C* **2007**, *111*, 15759.

[29] M. Marelli, F. Zaccheria, N. Ravasio, E. Pitzalis, Y. Didi, A. Galarneau, N. Scotti, C. Evangelisti, *Catalysts* **2023**, *13*, 341.
[30] R. Beucher, R. D. Andrei, C. Cammarano, A. Galarneau, F. Fajula, V. Hulea, *ACS Catal.* **2018**, *8*, 3636.
[31] A. Sachse, N. Linares, P. Barbaro, F. Fajula, A. Galarneau, *Dalton Trans.* **2013**, *42*, 1378.
[32] D. Balköse, U. Köktürk, H. Yilmaz, *Appl. Surf. Sci.* **1999**, *147*, 77.
[33] A. Sachse, R. Ameloot, B. Coq, F. Fajula, B. Coasne, D. De Vos, A. Galarneau, *Chem. Commun.* **2012**, *48*, 4749.
[34] X. Wen, B. Zhang, W. Wang, F. Ye, S. Yue, H. Guo, G. Gao, Y. Zhao, Q. Fang, C. Nguyen, X. Zhang, J. Bao, J. T. Robinson, P. M. Ajayan, J. Lou, *Nat. Mater.* **2021**, *20*, 1506.
[35] M. Thommes, K. Kaneko, A. V. Neimark, J. P. Olivier, F. Rodriguez-Reinoso, J. Rouquerol, K. S. W. Sing, *Pure Appl. Chem.* **2015**, *87*, 1051.

